International Journal of Innovative Computing, Information and Control
Volume **21**, Number **5**, October **2025**

ICIC International ©2025 ISSN 1349-4198
pp. **1209–1219**

IMPROVEMENT OF SPARSITY AVERAGING METHOD IN INTERFEROMETRIC STOKES IMAGING

Ratri Dwi Atmaja[1,3], Andriyan Bayu Suksmono[1], Donny Danudirdjo[1] and Taufiq Hidayat[2]

[1]School of Electrical Engineering and Informatics
[2]Faculty of Mathematics and Natural Sciences
Institut Teknologi Bandung
Jl. Ganesa No. 10, Bandung 40132, Indonesia
{ suksmono; donny; taufiq.hidayat }@itb.ac.id

[3]Telecommunication Engineering Study Program
School of Electrical Engineering
Telkom University
Main Campus (Bandung Campus), Jl. Telekomunikasi No. 1, Bandung 40257, West Java, Indonesia
ratridwiatmaja@telkomuniversity.ac.id

Received January 2025; revised May 2025

Abstract. *An interferometric radio telescope imaging system can produce an image of an observed astronomical object. In practice, the number of telescopes, baseline length, and atmospheric attenuation limit the measurements. As a result, the measurements are incomplete and corrupted with noise. To get a better image quality, we can apply a reconstruction method that relies on sparsity called polarized SARA (sparsity averaging reweighted analysis), which is combined with our new proposed parameter to speed up sparsity. By applying this method, the reconstruction results can be improved in terms of reduced number of iterations and increased image quality. In the experiments, compared with polarized SARA, the method can obtain results faster by an average of 49.35% iteration difference and better image quality by an average of 20.35% difference in signal quality.*

Keywords: Interferometric, High angular resolution, Image processing, Polarized SARA

1. **Introduction.** Signal processing is an important part of astronomical imaging using radio interferometry. It aims to obtain a reconstructed image from the results of a few samples. The number of telescopes N spread over various locations on the Earth affects the number of samples $N(N-1)$. The fewer telescopes used, the fewer sampling points that can be obtained. The number of telescopes, baseline length, and atmospheric attenuation affect the quality of the reconstructed image. The baseline is a straight line connecting two telescopes, as seen from the source. A longer baseline yields a higher angular resolution that can be obtained. However, the longest possible baseline is only along the diameter of the Earth. In addition, atmospheric attenuation causes the sampling results to be corrupted with noise.

In radio interferometry, we can use the compressive sensing (CS) method [1-6] to reconstruct an image based on only a few samples. Candes et al. [7] developed a reweighted ℓ_1 norm to reduce the solution space in the reconstruction process, which was effectively applied to radio interferometric imaging by [8]. Because it is more effective than ℓ_1 minimization, Carillo et al. [9-11] also used the reweighted ℓ_1 norm to Stokes I imaging, known

DOI: 10.24507/ijicic.21.05.1209

as sparsity averaging reweighted analysis (SARA). They proposed the SARA method relying on the assumption that astrophysical signals are sparse in many bases (Dirac basis or wavelet bases), so it becomes powerful when using average sparsity over multiple bases. Moreover, the SARA method is defined on the convex optimization framework, significantly enhancing the reconstruction speed. The SARA method performs better than some fast reconstruction methods with built-in signal sparsity and convex optimization frameworks. However, this SARA method can only be used on Stokes I imaging. This gap encourages the appearance of the following algorithm performing on one Stokes and others. Therefore, for use in polarimetric imaging, Birdi et al. [12,13] added polarization constraints and developed the joint algorithm in all Stokes images I, Q, U, and V by using an iterative primal-dual algorithm [14-20]. This joint algorithm, polarized SARA, also adopted the epigraphical projection-based splitting technique previously proposed by [21] to overcome the minimization problem with four constraints. The polarized SARA performs better than the ℓ_1 and total variation (TV) regularizations proposed by [22].

We note that several astronomical sources were found to have a structural change on shorter timescales [23]. Also, the next-generation radio interferometry will produce large amounts of data [13]. In the future, these encourage the need for a reconstruction method with a faster computation time, even if we have limited computing resources. The convex optimization-based reconstruction method deals with this condition and can support reconstruction with good speed. In this paper, we choose polarized SARA because the process comes from the convex optimization framework and supports imaging for Stokes I, linear, and circular polarization. However, developed for Stokes images I, Q, U, and V causes consume expensive computation time. This background motivates us to modify the code of polarized SARA to introduce a new parameter named μ value to perform Stokes I and linear polarization imaging faster. By adjusting this parameter, our results suggest better image quality can be obtained in fewer iterations. In the experiments, we demonstrate that we can get a better signal quality (SQ) in fewer iterations of polarized SARA.

2. **Polarized SARA.** By using polarized SARA method, we can get four Stokes images: I, Q, U, and V. These images have intensity distribution characteristics coming from the observed object. All these Stokes are real-valued. The radio emissions have a total intensity that is represented in Stokes I, while Stokes Q, U, and V are the polarization of electromagnetic radiations received from the observed object. Stokes Q and U are linear polarization while Stokes V is circular polarization. The four Stokes have the following relationship

$$\sqrt{Q^2 + U^2 + V^2} \leq I. \tag{1}$$

In the previous study on the polarized SARA method, this Stokes relationship was added as a constraint to determine the reconstruction results [12].

The discrete measurement results in radio interferometer are modeled as follows

$$Y = \Phi\left(\bar{S}\right) + E, \tag{2}$$

with $Y \in \mathbb{C}^{M\times 4}$ as the measurement result, $E \in \mathbb{C}^{M\times 4}$ as random additive noise, $\bar{S} = [\bar{s}_1, \bar{s}_2, \bar{s}_3, \bar{s}_4] \in \mathbb{R}^{N\times 4}$ as the Stokes matrix, and $\Phi : \mathbb{C}^{N\times 4} \to \mathbb{C}^{M\times 4}$ as the measurement operator. By this definition, Stokes I, Q, U, and V can be expressed as $\bar{s}_1, \bar{s}_2, \bar{s}_3, \bar{s}_4 \in \mathbb{R}^N$. Therefore, the polarization constraint in Equation (1) can be written as

$$\forall n \in \{1, \ldots, N\}, \quad -S_{n,1} + \|S_{n,2:4}\|_2 \leq 0, \tag{3}$$

with $S_{n,1}$ as the nth component of Stokes I and $S_{n,2:4}$ as the nth component of Stokes Q, U, and V. Birdi et al. [12] added a polarization constraint (3) to solve problem (2) in the polarized SARA method.

Overall, polarized SARA has the following minimization problem

$$\underset{S\in\mathbb{R}^{N\times 4}}{\text{minimize}}\, f(\Phi(S)) + g\left(\Psi^\dagger S\right) + f_{\mathbb{U}}(S) + f_{\mathbb{V}}(S). \tag{4}$$

In Equation (4), $f_{\mathbb{U}}(S)$ states that the Stokes matrix must be real, with $\mathbb{U} = \mathbb{R}^{N\times 4}$. Then, $f_{\mathbb{V}}(S)$ states that the Stokes matrix must meet the polarization constraint criterion $\sqrt{Q^2+U^2+V^2} \leq I$, with $\mathbb{V} = \left\{S \in \mathbb{R}^{N\times 4} | (\forall n \in \{1,\ldots,N\}) \|S_{n,2:4}\|_2 - S_{n,1} \leq 0\right\}$. After that, $f(\Phi(S))$ is a constraint to meet the problem modeling criteria in Equation (2), where $f(\Phi(S)) = f_{\mathbb{B}(Y,E)}(\Phi(S))$ with $\mathbb{B}(Y,E) = \{\Phi(S) \in \mathbb{C}^{M\times 4} : \|\Phi(S) - Y\|_2 \leq E\}$. Lastly, $g\left(\Psi^\dagger S\right)$ is a weighted ℓ_1 norm which is defined as follows:

$$g\left(\Psi^\dagger S\right) = \left\|\Psi^\dagger S\right\|_{W,1} = \sum_{i=1}^{4}\sum_{j=1}^{J} W_{j,i}\left|\left(\Psi^\dagger S\right)_{j,i}\right|. \tag{5}$$

In this equation, $(.)_{j,i}$ is the coefficient on the jth row and ith column of the argument, $W \in \mathbb{R}_+^{J\times 4}$ is the weighted matrix, $\Psi \in \mathbb{C}^{N\times J}$ is the dictionary, $\Psi^\dagger S$ is the sparse representation of signal S in the dictionary Ψ, and $\Psi^\dagger$ is the adjoint of Ψ. We might want to write a minimization problem using two constraints. In Equation (2), if we reconstruct the signal S from the degraded signal Y without considering $f_{\mathbb{U}}(S)$ and $f_{\mathbb{V}}(S)$, the minimization problem can be written as

$$\underset{S\in\mathbb{R}^{N\times 4}}{\text{minimize}}\, f(\Phi(S)) + g\left(\Psi^\dagger S\right) = \underset{S\in\mathbb{R}^{N\times 4}}{\text{minimize}} \left\|\Psi^\dagger S\right\|_{W,1} \text{ subject to } \|Y - \Phi(S)\|_2 \leq E, \tag{6}$$

or

$$\underset{S\in\mathbb{R}^{N\times 4}}{\text{minimize}}\ \mu\left\|\Psi^\dagger S\right\|_{W,1} + \frac{1}{2}\|Y - \Phi(S)\|_2^2. \tag{7}$$

Meanwhile, polarized SARA is a minimization problem with four constraints.

To solve the resultant minimization problem (4), Birdi et al. [12] proposed polarized SARA below.

Polarized SARA.

Input: $Y \in \mathbb{C}^{M\times 4}$

Output: $S \in \mathbb{R}^{N\times 4}$

1. initiate $\boldsymbol{S}^{(0)} \in \mathbb{R}^{N\times 4}$, $\boldsymbol{A}^{(0)} \in \mathbb{R}^{J\times 4}$, $\boldsymbol{B}^{(0)} \in \mathbb{R}^{M\times 4}$, $\boldsymbol{C}^{(0)} \in \mathbb{R}^{N\times 4}$, $\boldsymbol{D}^{(0)} \in \mathbb{R}^{N\times 2}$, $\boldsymbol{Z}^{(0)} \in \mathbb{R}^{N\times 2}$, $\gamma W \in \mathbb{R}_+^{J\times 4}$,
2. update the solution $\boldsymbol{S}^{(k+1)} = \mathcal{P}_{\mathbb{U}}\left(\boldsymbol{S}^{(k)} - \boldsymbol{\tau}\left(\boldsymbol{\Psi}\boldsymbol{A}^{(k)} + \boldsymbol{\Phi}^\dagger\left(\boldsymbol{B}^{(k)}\right) + \boldsymbol{C}^{(k)}\right)\right)$,
3. update $\boldsymbol{Z}^{(k+1)} = \mathcal{P}_{\mathbb{V}}\left(\boldsymbol{Z}^{(k)} - \boldsymbol{\tau}\boldsymbol{D}^{(k)}\right)$,
4. calculate $\hat{A}^{(k)} = \boldsymbol{A}^{(k)} + \rho_1\boldsymbol{\Psi}^\dagger\left(2\boldsymbol{S}^{(k+1)} - \boldsymbol{S}^{(k)}\right)$, then update $\boldsymbol{A}^{(k+1)} = \hat{A}^{(k)} - \rho_1\mathcal{T}_{\gamma W/\rho_1}\left(\frac{\hat{A}^{(k)}}{\rho_1}\right)$,
5. calculate $\hat{B}^{(k)} = \boldsymbol{B}^{(k)} + \rho_2\boldsymbol{\Phi}\left(2\boldsymbol{S}^{(k+1)} - \boldsymbol{S}^{(k)}\right)$, then update $\boldsymbol{B}^{(k+1)} = \hat{B}^{(k)} - \rho_2\mathcal{P}_{\mathbb{B}(Y,E/\rho_2)}\left(\frac{\hat{B}^{(k)}}{\rho_2}\right)$,
6. calculate $\hat{C}^{(k)} = \boldsymbol{C}^{(k)} + \rho_3\left(2\boldsymbol{S}^{(k+1)} - \boldsymbol{S}^{(k)}\right)$ and $\hat{D}^{(k)} = \boldsymbol{D}^{(k)} + \rho_3\left(2\boldsymbol{Z}^{(k+1)} - \boldsymbol{Z}^{(k)}\right)$,
7. calculate $\begin{pmatrix} C_{:,1}^{(k+1)} \\ D_{:,1}^{(k+1)} \end{pmatrix} = \begin{pmatrix} \hat{C}_{:,1}^{(k)} \\ \hat{D}_{:,1}^{(k)} \end{pmatrix} - \rho_3\mathcal{P}_{\mathbb{E}_1}\left(\frac{1}{\rho_3}\begin{bmatrix} \hat{C}_{:,1}^{(k)} \\ \hat{D}_{:,1}^{(k)} \end{bmatrix}\right)$ and $\begin{pmatrix} C_{:,2:4}^{(k+1)} \\ D_{:,2}^{(k+1)} \end{pmatrix} = \begin{pmatrix} \hat{C}_{:,2:4}^{(k)} \\ \hat{D}_{:,2}^{(k)} \end{pmatrix} - \rho_3\mathcal{P}_{\mathbb{E}_2}\left(\frac{1}{\rho_3}\begin{bmatrix} \hat{C}_{:,2:4}^{(k)} \\ \hat{D}_{:,2}^{(k)} \end{bmatrix}\right)$,

8. repeat steps 2 to 7 until convergence.

The primal stage updates function to update variables S and Z (steps 2 and 3). Meanwhile, the dual stage updates function to update variables A, B, C and D (steps 4 to 7). In step 2, $\mathcal{P}_{\mathbb{U}}(X)$ functions to retrieve the real part of X. Then, in step 3, $Z \in \mathbb{R}^{N\times 2}$ is a value to satisfy $f_{\mathbb{V}}(S)$ in the minimization problem (4). The $f_{\mathbb{V}}(S)$ states that the Stokes matrix must meet the polarization constraint criterion $\sqrt{Q^2+U^2+V^2} \leq I$, with $\mathbb{V} = \left\{S \in \mathbb{R}^{N\times 4} | (\forall n \in \{1,\ldots,N\}) - S_{n,1} + \|S_{n,2:4}\|_2 \leq 0\right\}$. We have $-S_{n,1} \leq Z_{n,1}$ and $\|S_{n,2:4}\|_2 \leq Z_{n,2}$ so that $Z_{n,1} + Z_{n,2} \leq 0$. If $\forall U \in \mathbb{R}^{N\times 2}$, $\mathcal{P}_{\mathbb{V}}(U) = \tilde{U}$ $(\forall n \in \{1,\ldots,N\})$, then $\tilde{U} \in \mathbb{R}^{N\times 2}$ is defined as follows:

$$\left(\tilde{U}_{n,1}, \tilde{U}_{n,2}\right) = \begin{cases} (U_{n,1}, U_{n,2}), & \text{if } U_{n,1} + U_{n,2} \leq 0, \\ \dfrac{1}{2}(U_{n,1} - U_{n,2}, U_{n,2} - U_{n,1}), & \text{otherwise.} \end{cases} \tag{8}$$

In step 4, Ψ is a basis that is used as the dictionary. The first basis uses a Dirac basis while the other eight use Daubechies wavelets Db1-Db8 as in [6,24]. Then, using soft-threshold $\gamma W \in \mathbb{R}_+^{M\times 4}$, $\mathcal{T}_{\gamma W/\rho_1}\left(\frac{\hat{A}^{(k)}}{\rho_1}\right)$ in step 4 is a soft-thresholding operation with the following definition

$$\left(\forall \hat{A} \in \mathbb{R}^{M\times 4}\right) \quad \mathcal{T}_{\gamma W/\rho_1}\left(\frac{\hat{A}^{(k)}}{\rho_1}\right) = H. \tag{9}$$

In this definition, $H \in \mathbb{R}^{M\times 4}$ is

$$(\forall i \in \{1,2,3,4\}) \quad H_{:,i} = prox_{\left(\rho_1^{-1}\gamma W\right)_{:,i}\|.\|_1}\left(\hat{A}_{:,1}\right), \tag{10}$$

with $j \in \{1,\ldots,M\}$, and then $H_{j,i}$ can be written as follows:

$$H_{j,i} = \begin{cases} -\hat{A}_{j,i} + \dfrac{\gamma W_{j,i}}{\rho_1}, & \text{if } \hat{A}_{j,i} < -\gamma W_{j,i}/\rho_1, \\ 0, & \text{if } -\gamma W_{j,i}/\rho_1 \leq \hat{A}_{j,i} \leq \gamma W_{j,i}/\rho_1, \\ \hat{A}_{j,i} - \dfrac{\gamma W_{j,i}}{\rho_1}, & \text{otherwise.} \end{cases} \tag{11}$$

Step 5 aims to satisfy the constraint $f(\Phi(S))$ in Equation (4), with $\mathcal{P}_{\mathbb{B}(Y,E/\rho_2)}\left(\frac{\hat{B}^{(k)}}{\rho_2}\right)$ defined as follows:

$$\mathcal{P}_{\mathbb{B}(Y,E/\rho_2)}\left(\frac{\hat{B}^{(k)}}{\rho_2}\right) = \begin{cases} \left[\dfrac{\theta\left(\frac{\hat{B}^{(k)}}{\rho_2} - Y\right)}{\left\|\frac{\hat{B}^{(k)}}{\rho_2} - Y\right\|_2}\right] + Y, & \text{if } \left\|\dfrac{\hat{B}^{(k)}}{\rho_2} - Y\right\|_2 > \theta, \\ \dfrac{\hat{B}^{(k)}}{\rho_2}, & \text{otherwise.} \end{cases} \tag{12}$$

In Equation (12), we have a radius $\theta = \frac{E}{\rho_2}$. E is the noise level that can be set by the user, and ρ_2 is as a constant value. Steps 6 and 7 aim to perform an epigraphical projection [21]. For $(c,d) \in \left(\mathbb{R}^N\right)^2$, in step 7, we have $\mathcal{P}_{\mathbb{E}_1}(c,d) = \left(\hat{c}_n, \hat{d}_n\right)_{1\leq n\leq N}$ with

$$\left(\hat{c}_n, \hat{d}_n\right) = \begin{cases} (c_n, d_n), & \text{if } c_n + d_n \geq 0, \\ \left(\dfrac{(c_n - d_n)}{2}, \dfrac{(d_n - c_n)}{2}\right), & \text{otherwise.} \end{cases} \tag{13}$$

Then, for $\left(R \in \mathbb{R}^{N\times 3}, d \in \mathbb{R}^N\right)$, in step 7, we have $\mathcal{P}_{\mathbb{E}_2}(R,d) = \left(\hat{R}_{n,:}, \hat{d}_n\right)_{1\leq n\leq N}$ with

$$\left(\hat{R}_{n,:}, \hat{d}_n\right) = \begin{cases} (0,0), & \text{if } \|R_{n,:}\|_2 < -d_n, \\ (R_{n,:}, d_n), & \text{if } \|R_{n,:}\|_2 < d_n, \\ \alpha_n(R_{n,:}, \|R_{n,:}\|_2), & \text{otherwise,} \end{cases} \tag{14}$$

and $\alpha_n = \frac{1}{2}\left(1 + \frac{d_n}{\|R_{n,:}\|_2}\right)$. Lastly, as in [19], the algorithm converges under the condition $\frac{1}{\tau} - \rho_1\|\Psi\|_{sp}^2 - \rho_2\|\Phi\|_{sp}^2 - \rho_3 \geq 0$, with the spectral norm denoted by $\|\cdot\|_{sp}$.

3. **Proposed Method.** In step 5, polarized SARA performs

$$\boldsymbol{B}^{(k+1)} = \hat{B}^{(k)} - \rho_2 \mathcal{P}_{\mathbb{B}(Y,E/\rho_2)}\left(\frac{\hat{B}^{(k)}}{\rho_2}\right)$$

to update $\boldsymbol{B}^{(k+1)}$. Our idea is to speed up the process by increasing $\mathcal{P}_{\mathbb{B}(Y,E/\rho_2)}\left(\frac{\hat{B}^{(k)}}{\rho_2}\right)$. We assume $\mu = \left\|\frac{\hat{B}^{(k)}}{\rho_2} - Y\right\|_2$ when calculating $\mathcal{P}_{\mathbb{B}(Y,E/\rho_2)}\left(\frac{\hat{B}^{(k)}}{\rho_2}\right)$, referring to Equation (12). Iteration by iteration at each Stokes, polarized SARA calculates this μ value. We note that this μ value is the second-order norm of the difference $\frac{\hat{B}^{(k)}}{\rho_2}$ and Y. We know that the constant ρ_2 and the measurement signal Y do not change in each iteration. So, we choose to increase $\hat{B}^{(k)}$ to make changes to update $\boldsymbol{B}^{(k+1)}$. To adjust $\hat{B}^{(k)}$, in polarized SARA, we added a constant a in step 5 so that the equations change to

$$\hat{B}^{(k)} = \boldsymbol{B}^{(k)} + a\rho_2\boldsymbol{\Phi}\left(2\boldsymbol{S}^{(k+1)} - \boldsymbol{S}^{(k)}\right), \tag{15}$$

and

$$\boldsymbol{B}^{(k+1)} = \hat{B}^{(k)} - a\rho_2 \mathcal{P}_{\mathbb{B}(Y,E/\rho_2)}\left(\frac{\hat{B}^{(k)}}{\rho_2}\right). \tag{16}$$

According to Equation (12) in step 5, note that $\mu = \left\|\frac{\hat{B}^{(k)}}{\rho_2} - Y\right\|_2$, increasing $\hat{B}^{(k)}$ without changing ρ_2 and Y indicates an increasing this μ value and SQ. To test these indicators, we use the forward-jet model image [26,27] to check the preliminary reconstruction results on Stokes I imaging during 2,000 iterations. This image has a size of 100×100 pixels. Measurement is done using realistic u-v coverage in the top left panel of Figure 1. This measurement is claimed to be under the real conditions on a VLBI array with six stations [22,25]. In this preliminary reconstruction results, in the bottom left and bottom right panel of Figure 1, the μ value will increase and the residual value will decrease if the value of a increases.

Presented by [28], in convex optimization, we note that the residual value affects the convergence rate. The faster the residual value reaches a minimum, the faster the convergence. It showed fewer iteration or computation time when it got minimum residual value faster. In our results, in the top right panel of Figure 1, the signal quality (SQ) of $a = 15, 25, 50$ reaches a plateau when the residual value already minimum. We estimate that polarized SARA ($a = 1$) will still reach a same plateau, so using $a > 1$, we can get a similar SQ faster than polarized SARA. We then test this hypothesis on the simulated data used by [12,22]. In Figure 1, we use the definition of signal quality (SQ) as follows:

$$SQ = 20\log_{10}\left(\frac{\left\|\hat{S}\right\|_2}{\left\|S - \hat{S}\right\|_2}\right), \tag{17}$$

with $\hat{S}$ as the true image and S as the corresponding reconstructed image. Higher SQ indicates better quality.

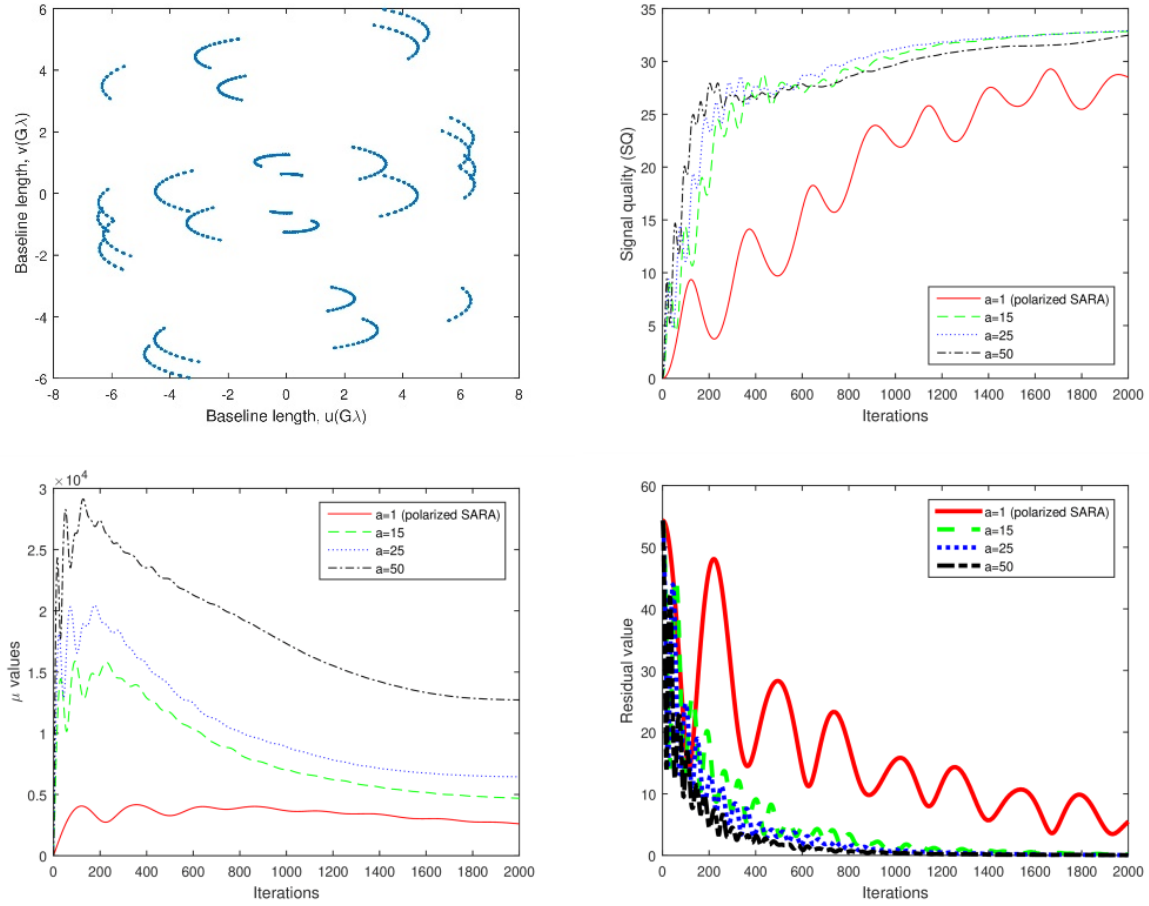

FIGURE 1. First row shows u-v coverage used in [12,22,25] and SQ results of the forward-jet model in Stokes I image using $a = 1, 15, 25, 50$ during 2,000 iterations. Second row shows the μ values and the residual values of the forward-jet model in Stokes I image using $a = 1, 15, 25, 50$ during 2,000 iterations.

4. **Results.** In simulation, we use two models of ground truth images (shown in the left column of Figure 2) to numerically simulate the M87 horizon-level shape measurements based on certain parameters and then evaluate the reconstruction results based on these ground truth images. The first ground truth image is named forward-jet model image in [12], and was presented in [27] and previously proposed in [26]. The second ground truth image is named counter-jet model image in [12], and was constructed in [29] based on general relativistic magneto-hydrodynamic. For these two models, we choose the image with size of 100×100 pixels. Then, we consider field of view of 200 μas so the scale of event horizon radius is corresponded to a resultant pixel size of 2 μas. We use the noisy measurements on Equation (2) while the measurement operator is defined by

$$\Phi\left(\bar{S}\right) = \varphi \bar{S} L, \tag{18}$$

with $\varphi = GFZ$. An operator $L \in \mathbb{C}^{4\times 4}$ functions to give the brightness matrix on the Stokes matrix $\bar{S}$. Then, the image located in each column of the brightness matrix $\bar{S}L$ is oversampled by a zero padding operator $Z \in \mathbb{C}^{\alpha N \times N}$ with a factor of α in each dimension. Once the oversampled images obtained, a matrix $F \in \mathbb{C}^{\alpha N \times \alpha N}$ is used to act fast Fourier transform on the oversampled images that are sampled by the interferometer. We then have a matrix $G \in \mathbb{C}^{M \times \alpha N}$ to degrade the discrete Fourier coefficients to the continuous

samples. We use scaling and oversampling in the matrix Z because the matrix G may have the interpolation errors. With these simulation settings, we perform measurements on the realistic u-v coverage in Figure 1. We consider a Gaussian noise with $\sigma = 5 \times 10^{-3}$ Jansky to corrupt each column of the brightness matrix $\bar{S}L$. We can determine a radius or a noise bound E in Equations (6) and (12) from the σ as $E^2 = \frac{\sigma^2}{2}\left[8M + 2\sqrt{2(8M)}\right]$.

In the top right panel of Figure 1, we have SQ results of the forward-jet model image using $a = 1, 15, 25, 50$ during 2,000 iterations. In this figure, we want to compare the existing polarized SARA method $a = 1$ with the proposed method $a = 15, 25, 50$. As for $a = 15, 25, 50$, the results show that SQ are increasing with 200-300 iterations and reach some plateau afterwards with similar SQ results. We predict the SQ of $a = 1$ can still increase and also reach the similar SQ because its residual value in the bottom right panel of Figure 1 has not reached a minimum level. Then, we deliver the SQ result of $a = 1$ on more iterations compared with $a = 50$ to take the best SQ of this both a value. A best SQ is taken when it does not change more than 1 percent within next 100 s iterations indicating reaching a plateau. We choose $a = 50$ to compare with $a = 1$ because it has a higher SQ in early iterations than $a = 15, 25$ and a higher SQ graph slope at iterations approaching 2,000. In Table 1, we perform not only for the forward-jet model but also the counter-jet model, including Stokes I image and linear polarization image.

TABLE 1. SQ does not change more than 1 percent within next 100 s iterations: The forward-jet model and the counter-jet model.

Forward-jet model						
Image	**SQ**			**Iteration**		
	$a = 1$	$a = 50$	**Difference**	$a = 1$	$a = 50$	**Difference**
Stokes I	28.15	27.84	-1.1%	2,152	590	72.58%
Linear polarization	17.86	25.79	44.4%	541	308	43.07%
Counter-jet model						
Image	**SQ**			**Iteration**		
	$a = 1$	$a = 50$	**Difference**	$a = 1$	$a = 50$	**Difference**
Stokes I	12.79	15.22	19.00%	1,371	708	48.36%
Linear polarization	12.94	15.41	19.09%	1,302	867	33.41%

Observing the SQ and iteration results on Stokes I image of the forward-jet model reconstruction in Table 1, we have the similar SQ among $a = 1, 50$ but fewer iteration using $a = 50$. The consistent result in getting fewer iteration is also obtained for the counter-jet model reconstruction on Stokes I image. Moreover, we have a higher SQ result 2.43 dB or 19.00% when using $a = 50$. We then can observe the SQ and iteration results on linear polarization image of both the forward-jet and the counter-jet model reconstruction in Table 1. Compared with $a = 1$, it shows not only fewer iteration but also higher SQ when using $a = 50$.

To see visual comparison of these tests, we present Stokes I and linear polarization intensity image between ground truth image, reconstruction result using $a = 1$, and $a = 50$ in Figure 2. The first column shows the ground truth image, whereas the second and third columns show the results for $a = 1$ and $a = 50$, respectively. The reconstructed images using $a = 1$ and $a = 50$ are taken based on the SQ results in Table 1. Comparing between using $a = 1$ and $a = 50$ in Stokes I intensity image of the forward-jet model in the first row of Figure 2, we can see that the hole formed clearer when using $a = 50$ although it has the lower SQ of 0.31 dB or 1.1%. The clearer hole result also appears in Stokes I intensity image of the counter-jet model in the third row of Figure 2. Then, if

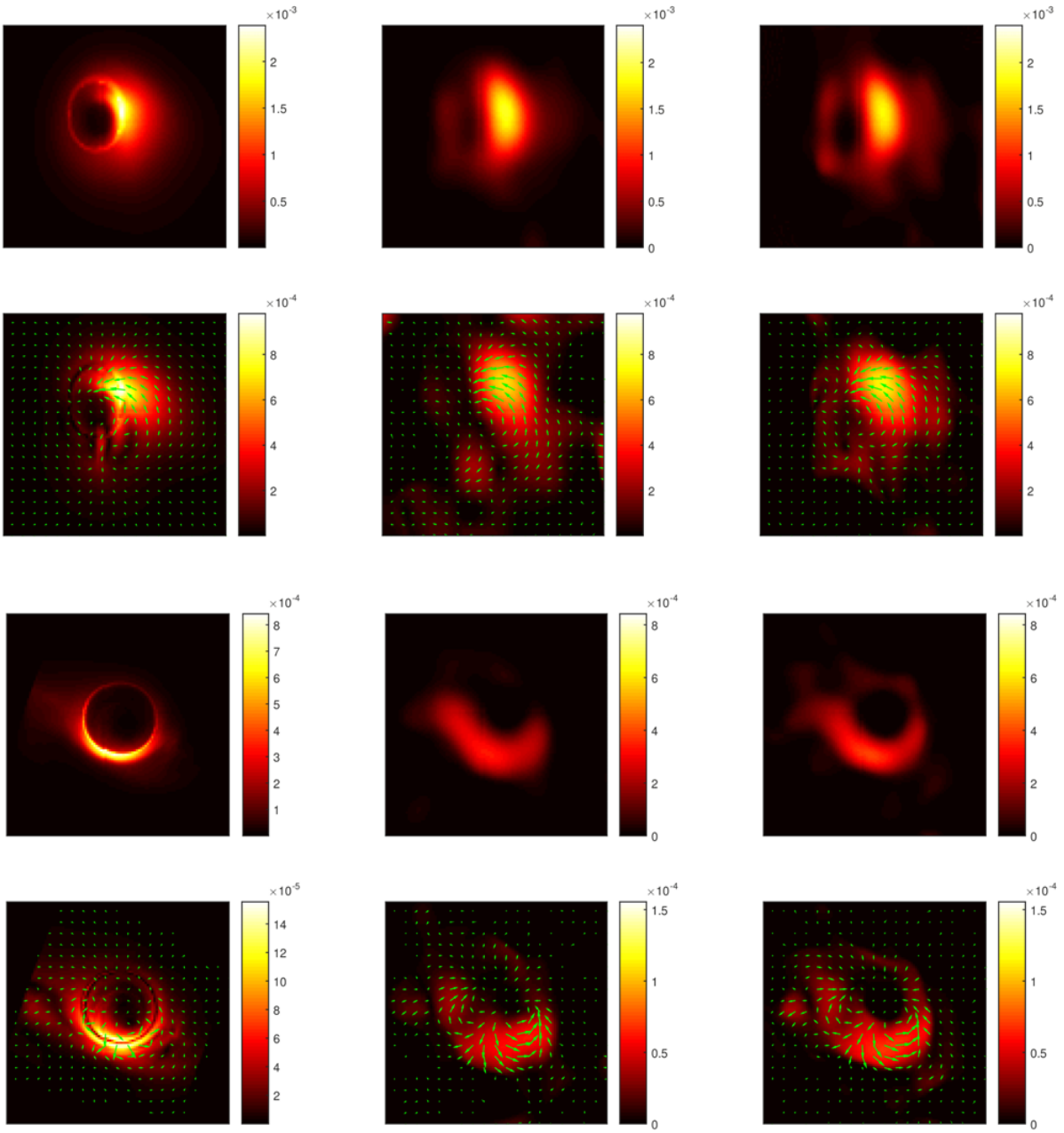

FIGURE 2. Reconstruction results of simulated data. Left to right: ground truth image, $a = 1$, and $a = 50$. The first and second rows are Stokes I and linear polarization intensity image of the forward-jet model while the third and fourth rows are from the counter-jet model. The electric vector polarization angle (EVPA) overlays on the linear polarization intensity image, shown by the green bars.

we observe the difference in linear polarization intensity image, the hole of the forward-jet model in the second row of Figure 2 starts appearing when using $a = 50$. Significantly better hole result is also seen on the counter-jet model in the fourth row of Figure 2.

5. **Conclusion.** This paper contributes to radio interferometry imaging in terms of obtaining a better quality of image with a significant fewer number of iterations by adjusting the μ value of polarized SARA. This μ value can be adjusted by adjusting the value of

a in Equations (15) and (16). In testing the data, after comparing the image results and the number of iterations between our proposed method and the polarized SARA, both in Stokes I and linear polarization intensity, our proposed method is proven to get the improved image in fewer iterations. The image has the shape of hole clearer. Because of the ability to reduce number of iterations, our proposed method probably has the speed at which the convergence to the SQ is achieved. The level of residual value may influence this convergence. This topic becomes an important challenge in future work. In addition, Polca SARA [30] that presents a global convergence guarantees may also be adopted to improve the quality.

REFERENCES

[1] A. B. Suksmono, Deconvolution of VLBI images based on compressive sensing, *2009 International Conference on Electrical Engineering and Informatics*, vol.1, pp.110-116, 2009.

[2] Y. Wiaux, L. Jacques, G. Puy, A. M. Scaife and P. Vandergheynst, Compressed sensing imaging techniques for radio interferometry, *Monthly Notices of the Royal Astronomical Society*, vol.395, no.3, pp.1733-1742, 2009.

[3] Y. Wiaux, G. Puy and P. Vandergheynst, Compressed sensing reconstruction of a string signal from interferometric observations of the cosmic microwave background, *Monthly Notices of the Royal Astronomical Society*, vol.402, no.4, pp.2626-2636, 2010.

[4] F. Li, T. J. Cornwell and F. de Hoog, The application of compressive sampling to radio astronomy-I: Deconvolution, *Astronomy & Astrophysics*, vol.528, no.31, 2011.

[5] H. Garsden, J. Girard, J.-L. Starck, S. Corbel, C. Tasse, A. Woiselle, J. McKean, A. S. van Amesfoort, J. Anderson, I. Avruch et al., Lofar sparse image reconstruction, *Astronomy & Astrophysics*, vol.575, no.90, 2015.

[6] A. Onose, R. E. Carrillo, A. Repetti, J. D. McEwen, J.-P. Thiran, J.-C. Pesquet and Y. Wiaux, Scalable splitting algorithms for big-data interferometric imaging in the SKA era, *Monthly Notices of the Royal Astronomical Society*, vol.462, no.4, pp.4314-4335, 2016.

[7] E. J. Candes, M. B. Wakin and S. P. Boyd, Enhancing sparsity by reweighted L1 minimization, *Journal of Fourier Analysis and Applications*, vol.14, no.5, pp.877-905, 2008.

[8] A. Onose, A. Dabbech and Y. Wiaux, An accelerated splitting algorithm for radio-interferometric imaging: When natural and uniform weighting meet, *Monthly Notices of the Royal Astronomical Society*, vol.469, no.1, pp.938-949, 2017.

[9] R. E. Carrillo, J. D. McEwen and Y. Wiaux, Sparsity Averaging Reweighted Analysis (SARA): A novel algorithm for radio-interferometric imaging, *Monthly Notices of the Royal Astronomical Society*, vol.426, no.2, pp.1223-1234, 2012.

[10] R. E. Carrillo, J. D. McEwen, D. van de Ville, J.-P. Thiran and Y. Wiaux, Sparsity averaging for compressive imaging, *IEEE Signal Processing Letters*, vol.20, no.6, pp.591-594, 2013.

[11] R. E. Carrillo, J. D. McEwen and Y. Wiaux, Purify: A new approach to radio-interferometric imaging, *Monthly Notices of the Royal Astronomical Society*, vol.439, no.4, pp.3591-3604, 2014.

[12] J. Birdi, A. Repetti and Y. Wiaux, Sparse interferometric stokes imaging under the polarization constraint (polarized SARA), *Monthly Notices of the Royal Astronomical Society*, vol.478, no.4, pp.4442-4463, 2018.

[13] J. Birdi, A. Repetti and Y. Wiaux, Scalable algorithm for polarization constrained sparse interferometric stokes imaging, *2018 IEEE 10th Sensor Array and Multichannel Signal Processing Workshop (SAM)*, Sheffield, UK, pp.465-469, https://doi.org/10.1109/SAM.2018.8448968, 2018.

[14] A. Chambolle and T. Pock, A first-order primal-dual algorithm for convex problems with applications to imaging, *Journal of Mathematical Imaging and Vision*, vol.40, no.1, pp.120-145, 2011.

[15] P. L. Combettes and J.-C. Pesquet, Fixed-point algorithms for inverse problems in science and engineering, in *Springer Optimization and Its Applications*, Springer, 2011.

[16] L. Condat, A primal-dual splitting method for convex optimization involving Lipschitzian, proximable and linear composite terms, *Journal of Optimization Theory and Applications*, vol.158, no.2, pp.460-479, 2013.

[17] C. Vũ, A splitting algorithm for dual monotone inclusions involving cocoercive operators, *Advances in Computational Mathematics*, vol.38, no.3, pp.667-681, 2013.

[18] P. L. Combettes, L. Condat, J.-C. Pesquet and C. Vũ, A forward-backward view of some primal-dual optimization methods in image recovery, *2014 IEEE International Conference on Image Processing (ICIP)*, pp.4141-4145, 2014.
[19] J.-C. Pesquet and A. Repetti, A class of randomized primal-dual algorithms for distributed optimization, *J. Nonlinear Convex Anal.*, vol.16, pp.2453-2490, 2015.
[20] N. Komodakis and J.-C. Pesquet, Playing with duality: An overview of recent primal dual approaches for solving large-scale optimization problems, *IEEE Signal Processing Magazine*, vol.32, no.6, pp.31-54, 2015.
[21] G. Chierchia, N. Pustelnik, J.-C. Pesquet and B. Pesquet-Popescu, Epigraphical projection and proximal tools for solving constrained convex optimization problems, *Signal, Image and Video Processing*, vol.9, pp.1737-1749, 2015.
[22] K. Akiyama, S. Ikeda, M. Pleau, V. L. Fish, F. Tazaki, K. Kuramochi, A. E. Broderick, J. Dexter, M. Mo'scibrodzka, M. Gowanlock et al., Superresolution full-polarimetric imaging for radio interferometry with sparse modeling, *The Astronomical Journal*, vol.153, no.4, 159, 2017.
[23] K. L. Bouman, M. D. Johnson, A. V. Dalca, A. A. Chael, F. Roelofs, S. S. Doeleman and W. T. Freeman, Reconstructing video of time-varying sources from radio interferometric measurements, *IEEE Transactions on Computational Imaging*, vol.4, no.4, pp.512-527, 2018.
[24] S. Mallat, *A Wavelet Tour of Signal Processing*, Elsevier, 1999.
[25] K. Akiyama, K. Kuramochi, S. Ikeda, V. L. Fish, F. Tazaki, M. Honma, S. S. Doeleman, A. E. Broderick, J. Dexter, M. Mo'scibrodzka et al., Imaging the Schwarzschild-radius-scale structure of M87 with the event horizon telescope using sparse modeling, *The Astrophysical Journal*, vol.838, no.1, 2017.
[26] A. E. Broderick and A. Loeb, Imaging the black hole silhouette of M87: Implications for jet formation and black hole spin, *The Astrophysical Journal*, vol.697, no.2, 1164, 2009.
[27] R.-S. Lu, A. E. Broderick, F. Baron, J. D. Monnier, V. L. Fish, S. S. Doeleman and V. Pankratius, Imaging the supermassive black hole shadow and jet base of M87 with the event horizon telescope, *The Astrophysical Journal*, vol.788, no.2, 120, 2014.
[28] X. Chang, J. Yang and H. Zhang, A convex combination based primal-dual algorithm with linesearch for general convex-concave saddle point problems, *arXiv Preprint*, arXiv: 2401.08211, 2024.
[29] J. Dexter, J. C. McKinney and E. Agol, The size of the jet launching region in M87, *Monthly Notices of the Royal Astronomical Society*, vol.421, no.2, pp.1517-1528, 2012.
[30] J. Birdi, A. Repetti and Y. Wiaux, Polca SARA-Full polarization, direction dependent calibration, and sparse imaging for radio interferometry, *Monthly Notices of the Royal Astronomical Society*, vol.492, no.3, pp.3509-3528, 2020.

Author Biography

Ratri Dwi Atmaja received the ST degree in Telecommunication Engineering from Institut Teknologi Telkom (now Telkom University), Indonesia, 2009; the MT degree in Electrical-Telecommunication Engineering from Institut Teknologi Telkom, Indonesia, 2011; the Dr degree in Electrical Engineering and Informatics, from Institut Teknologi Bandung, Indonesia, 2025. He is currently a full-time Lecturer at the School of Electrical Engineering, Telkom University, Indonesia. His research interests include compressive sensing, imaging, and signal processing.

Andriyan Bayu Suksmono received the B.S. degree in Physics and the M.S. degree in Electrical Engineering from the Institut Teknologi Bandung (ITB), Indonesia, and the Ph.D. degree in Engineering from the University of Tokyo, Japan, in 1990, 1996 and 2002, respectively. He joined ITB as an Instructor (1996-2005), Associate Professor (2005-2009), and Professor (2009-present) at the School of Electrical Engineering and Informatics, ITB, Indonesia. His main research interests are signal processing and imaging. He is a Professional Member of the ACM. He has been granted several international research funds, scholarships, and fellowship, from RCAST-Tokyo University, Monbukagakusho, JSPS, AIGRP, and the Hitachi Foundation.

Donny Danudirdjo received the bachelor's and master's degrees in Electrical Engineering from Institut Teknologi Bandung (ITB), Indonesia, in 2005 and 2007, respectively, and the Ph.D. degree in Electrical Engineering from the University of Tokyo, Japan, in 2013. He is currently a Lecturer with the Research Group of Biomedical Engineering, School of Electrical Engineering and Informatics, ITB, Indonesia. His research interests include medical imaging and signal processing.

Taufiq Hidayat received bachelor's degree in Astronomy from Institut Teknologi Bandung (ITB), Indonesia, in 1989. His master's and Ph.D. degrees in Astrophysics were received from Université Paris Diderot, Sorbonne Paris Cité, France, in 1993 and 1997, respectively. He has served as Head of the Astronomy Department ITB (1999-2004), Director of Bosscha Observatory (2006-2010), and currently he is Head of the Astronomy Research Division in the Faculty of Mathematics and Natural Sciences at ITB. His interest is in millimeter/submillimeter radio astronomical observations of planetary atmospheres. Recently, he joined a sub-Working Group for star-formation of the East-Asian VLBI Network, and a research group to study the deep field environment of radio galaxies using ALMA data.